Contents lists available at ScienceDirect

Applied Catalysis B: Environmental

Assemblies of nanoparticles of CeO_2–ZnTi-LDHs and their derived mixed oxides as novel photocatalytic systems for phenol degradation

E.M. Seftel [a,*], M.C. Puscasu [b], M. Mertens [c], P. Cool [a], G. Carja [b,**]

[a] Laboratory of Adsorption and Catalysis, Department of Chemistry, University of Antwerpen (CDE), Universiteitsplein 1, 2610 Wilrijk, Antwerpen, Belgium
[b] Department of Chemical Engineering, Faculty of Chemical Engineering and Environmental Protection, Technical University "Gh. Asachi" of Iasi, Bd. D. Mangeron, 700554 Iasi, Romania
[c] VITO Flemish Institute for Technological Research, Boeretang 200, B-2400, Belgium

ARTICLE INFO

ABSTRACT

Self-assemblies of nanoparticles of CeO_2/ZnTi layered double hydroxides (CeO_2/ZnTi-LDH) and the derived CeO_2/Zn_2TiO_4 systems are reported as novel efficient nano-photocatalysts for phenol degradation. The spontaneous formation and organization of nanoparticles of CeO_2 on ZnTi-LDH matrix is based on a cheap, nontoxic and facile technique that invokes the manifestation of the structural memory effect of LDH in aqueous solution of $Ce(SO_4)_2$. It was found that the composition of the brucite-type layer has a major effect on establishing the performances of the phenol photodegradation process. Moreover the LDH layered matrix offers multiple advantages, such as manipulation of the brucite-like layer composition and the insertion of key cations, like Zn^{2+} and Ti^{4+}, but also the possibility to supply a good dispersion of the metal cations within the layers, which may act as charge separation centers enhancing the efficiency in subsequent applications. These results open new opportunities in the development of hybrid nano-assemblies systems able to utilize their collective properties for facilitating cumulative photocatalytic properties for "green" removal of dangerous pollutants.

1. Introduction

The increasing environmental problems due to water pollution by industrial effluents have driven considerable research efforts on pollutant degradation by heterogeneous photocatalysis [1]. Phenol and phenolic compounds are major pollutants of aquatic environment. Phenol may occur in aquatic environment due to its widespread use in agricultural, petrochemical, textile, paint, plastic and pesticide chemical industries. Defined by a high carcinogenic and mutagenic potential, phenol poses a high risk to mammalian and aquatic life [2]. Owing to its stability and solubility in water, its removal to a safety level (0.1–1.0 mg/L) is a difficult process [3]. Consequently, a growing interest exists nowadays to develop new photocatalysts able to use the light energy for generating strongly oxidizing hydroxyl radicals (•OH), which oxidize not only phenol but also a broad range of organic pollutants from wastewaters [4,5]. The use of nanocrystalline semiconductors as photocatalysts, to initiate interfacial redox reactions, have generated great interest, due to their unique physicochemical properties, caused by their nanosized dimensions and large surface/volume ratios.

Cerium oxide (CeO_2) is one of the most reactive rare earth metal oxides and has a broad range of applications in catalysis, electrochemistry or optics [6]. CeO_2 exhibits a strong absorption in the UV range and shows photocatalytic response mainly based on two features: due to its low redox potential a Ce ion can easily pass from Ce^{4+} to Ce^{3+} and, secondly, due to its high capacity to store oxygen [7]. Compared to TiO_2, cerium oxide has an absorption spectrum shifted 80 nm toward visible section of the visible spectrum [8]. Furthermore, the photogenerated electron–hole pairs were reported to have much longer lifetimes than those generated in TiO_2 [8]. However, comparable to pure TiO_2, the use of single CeO_2 acting as functional material always encounters some disadvantages. The pure CeO_2 is known to be poorly thermostable and undergoes rapid sintering under high temperatures, this greatly decreasing its oxygen storage capacity [9]. In order to overcome these problems, different approaches can be used. An approach may be the substitution of another metal or metal oxide into the original metal oxide lattice facilitating the formation of mixed oxides [9,10]. The formation of CeO_2–TiO_2 mixtures has been reported to improve the photocatalytic activity of the latter [7,9,11]. Another possibility to enhance the photocatalytic activity is to impregnate CeO_2 on adequate supports which may offer the opportunity not only to improve its performance but also to form new stable compounds

which lead to totally different physical and chemical properties from the individual components.

Song et al. studied the photocatalytic degradation of C.I. Direct Red 23 (4BS) in aqueous solutions under UV irradiation by the $SrTiO_3/CeO_2$ nanocomposite. They found that the $SrTiO_3/CeO_2$ powders had more photocatalytic activity for decolorization of 4BS than that of pure $SrTiO_3$ powder under UV irradiation [12]. Aguila et al. studied the effect of the support, Al_2O_3, ZrO_2, and SiO_2, on the activity for CO oxidation of a series of CuO and CeO_2 concluding that the nature of the support has a strong influence on the activity of the obtained materials, SiO_2 supported catalyst showing the higher activity [13]. On the other hand, the degradation of phenol by CeO_2 impregnated Al-MCM-41 was reported to be less efficient than benchmark Degussa P-25 TiO_2 [6]. Further, there is a strong interest nowadays to narrow the band gaps of photocatalysts thus to increase their photocatalytic response, by assembling different nanostructures rather than by incorporating dopant atoms [14]. Therefore an interesting and suitable possibility is to ensemble nanosized cerium oxide and layered double hydroxide (LDHs) type materials. Layered double hydroxides are a class of naturally occurring anionic clays. Their structure originates from the isomorphous substitution of divalent cations by trivalent or tetravalent cations in a brucite-like lattice leading to the formation of positively charged layers which are held together by the interlayer counter anions as well as by water molecules [4,15,16]. Layered double hydroxides are described by the general formula $[M^{II}_{1-x}M^{III}_x(OH)_2]^{x+} A^{n-}_{x/n} \cdot mH_2O$, where M^{II} and M^{III} are the divalent and trivalent cations forming the brucite-like sheets and A^{n-} are the anions which are located within the interlayer gallery together with the water molecules [17]. Layered double hydroxides have a number of advantages over other materials for environment remediation applications, as they are nontoxic, cheap and easy to prepare. These materials are currently employed on a wide scale as catalysts and catalyst precursors in fine organic syntheses [17] as well as for the oxidation of organic compounds in wastewaters [4,5,15,16,18]. Recently, CeO_2 supported LDHs have been studied for the semiconductive properties and their potential in photocatalytic degradation of some chlorophenolic compounds [19]. The study reports the possible formation of some intermediary organic molecules but a clear mineralization pathway still needs to be in-depth investigated. The aim of this work is to report the synthesis and characterization of the nanostructured assemblies of ceria – ZnTi-LDHs and the derived mixed oxides as novel nano-photocatalysts for phenol photodegradation under UV light. The structural, phase transformation in temperature and semiconducting properties of the obtained ceria supported materials are determined by XRD, TG/DTG, Raman and UV–vis DR spectroscopy techniques. Furthermore, the mechanism of phenol photodegradation is investigated. UV–vis spectroscopy is employed to rationalize the result of the photocatalytic degradation process.

2. Experimental details

2.1. Synthesis of the ZnTi-LDH support

The layered double hydroxide support containing Zn^{2+} and Ti^{4+} with the cationic ratio of 3 was prepared by a co-precipitation method at constant pH [17]. As for the standard procedure, the sample was prepared by the slow addition of a mixed $Zn(NO_3)_2 \cdot 6H_2O$ (Acros Organics, 98%) and $TiCl_4$ (Aldrich, 99.9%) solution (1 M in total) to a Na_2CO_3 (2×10^{-3} M) solution under magnetic stirring. During the synthesis the pH value was kept constant at 7.5 by adding suitable amounts of 2 M NaOH solution. The resulting slurry was aged about 24 h at room temperature. The final product was

recuperated by filtration, washed several times with distilled water and dried at room temperature.

2.2. Synthesis of the CeO2/ZnTi-LDH and the derived mixed oxide systems

1 g of the "freshly" calcined Zn-TiLDH (550 °C for 14 h) was added, under very vigorous stirring, at 250 ml of a 0.1 M aqueous solution of $Ce(SO_4)_2 \cdot 4H_2O$ (Aldrich, ≥98%) such that the final pH value of the reconstructed medium was ~9. The obtained samples were aged at ambient temperature for 45 min, washed, centrifuged, dried under vacuum and denoted as CeO_2/ZnTi-LDH. After calcinations at different temperatures up to 750 °C for 8 h the samples were denoted as CeO_2/ZnTi-T°C were T stands for the calcination temperature.

2.3. Photocatalytic experiments

The photocatalytic activity of both ZnTi-LDH, CeO_2/ZnTi-LDH and the derived mixed oxides obtained by calcination at different temperatures were tested for the photodegradation of phenol in aqueous solution.

Appropriate amounts of a catalyst were dispersed into a phenol solution (50 mg/L) in a batch reactor at an optimal catalyst dose of 0.5 g/L. The temperature was kept constant at 25 °C, and the solutions were stirred in dark for 30 min in order to reach the adsorption–desorption equilibrium between the dye and the catalyst surface. Afterward, the solutions were irradiated with UV-light for 7 h by using a UV Pen-Ray Power Supply (UVP Products) placed in a quartz tube, which was immersed in the solution. The phenol photodegradation profile was monitored by measuring UV–vis absorption spectra on a Jasco V550 spectrophotometer.

2.4. Characterization techniques

The structure and the crystal phases of the as synthesized solids were investigated by X-ray diffraction (XRD), FT-Raman, UV–vis diffuse reflectance spectroscopy (UV–vis-DR), and TG/DTA methods.

X-ray diffractions were recorded on a PANalytical X'Pert PRO MPD diffractometer with filtered CuKα radiation; measurements were done in the 2θ mode using a bracket sample holder with a scanning speed of 0.04°/4 s in continuous mode. Scanning electron microscopy (SEM) images were recorded on a Mira Tescan Type Mira II LMU Electronic Microscope. Transmission electron microscopy (TEM) images were performed on a Hitachi H99 transmission electron microscope operating at an accelerating voltage of 200 kV, coupled with energy dispersive X-ray (EDX) spectrometer. Raman spectra were measured on a Nicolet Nexus 670 bench equipped with a Ge detector in a 180° reflective sampling configuration using a 1064 nm Nd:YAG laser. UV–vis-DR spectra were obtained at room temperature on a NICOLET EVOLUTION 500 UV–vis Spectrometer, with a diffuse reflectance accessory using KBr standard white as reflectance. Thermoanalytical measurements were performed on a Mettler Toledo TGA/SDTA851^e thermobalance. Samples were heated at a heating rate of 5 °C/min under O_2 flow.

3. Results and discussion

3.1. Structural characterization of the catalysts

Layered double hydroxide containing zinc and titanium was prepared using the co-precipitation method at constant pH. This material is composed of ZnO_6 and TiO_6 octahedra and we rely on the hypothesis that upon calcination it is possible to obtain intimately
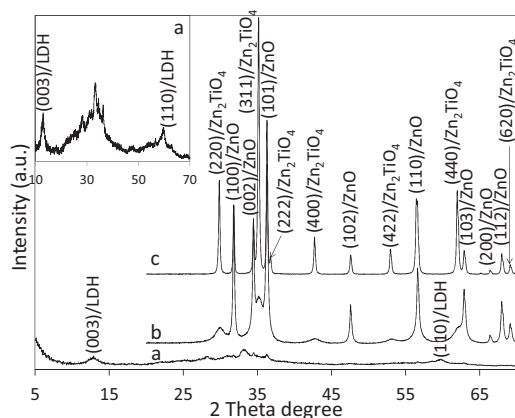
Fig. 1. The XRD patterns of the (a) ZnTi-LDH, (b) ZnTi-600 °C and (c) ZnTi-750 °C samples. For clarity, the enlargement of the pattern (a) is presented in the inset picture.
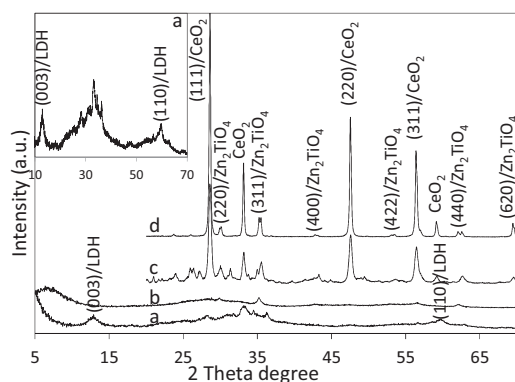

Fig. 2. The XRD patterns of the (a) ZnTi-LDH, (b) CeO_2/ZnTi-LDH, (c) CeO_2/ZnTi-600 °C and (d) CeO_2/ZnTi-750 °C samples. For clarity, the enlargement of the pattern (a) is presented in the inset picture.

dispersed mixed oxides that can behave as semiconductors with remarkable photo-oxidative responses. Furthermore, the immobilization of the CeO_2 nanoparticles on the surface of the ZnTi-LDH type material by taking advantage of the remarkable *memory effect* property of this type of material may represent a new, cheap and fast approach to obtain complex photocatalysts in mutual contact within atomic dimensions.

The XRD patterns of the as-synthesized ZnTi-LDH and the CeO_2/ZnTi-LDH catalysts together with the derived mixed oxides obtained by its calcination at different temperatures are presented in Figs. 1 and 2, respectively. Under the present experimental conditions, the ZnTi-LDH synthesis at room temperature allowed us to prepare a starting material characterized by very small crystallites (pattern (a) in Figs. 1 and 2, also enlarged for better clarity). Using the Scherrer equation [20] the crystallite sizes were calculated and the data are presented in Table 1. From the characteristic (0 0 3) and (1 1 0) peaks, the unit cell parameters c and a were estimated as 2.057 nm and 0.31 nm, respectively. Our previous results

obtained for the ZnAl-LDH type materials indicated that, for a cationic ratio of 3, the obtained unit cell parameters c and a were 2.36 nm and 0.306 nm, respectively [18,20]. The present results reveal that decreased interlayer distance, reflected by the c unit cell parameter, and increased cation–cation distance in the brucite-like layers, reflected by the a unit cell parameter [20], indicates that the obtained material incorporated the Ti^{4+} cations within the brucite-like network forming the characteristic layered structure [21].

Fig. 3A–C shows the SEM and TEM images of the ZnTi-LDH sample before and after the reconstruction process. The SEM image of the initial ZnTi-LDH sample shows the characteristic LDH morphology consisting of interconnected hexagonal platelet-like particles with mean average size of 400 nm. After the reconstruction step, the obtained CeO_2/ZnTi-LDH sample preserves the platelet-like morphology, but with an decreased mean average size of 150 nm (Fig. 3B). The decreased particle size observed for the CeO_2/ZnTi-LDH sample may be assigned to the reconstruction process which undergoes through a dissolution–recrystallization mechanism thus the obtained material being characterized by smaller average size of the LDH platelets. The SEM micrographs also reveal the uniformity in platelets sizes for both ZnTi-LDH as well CeO_2/ZnTi-LDH samples. Moreover, the SEM observations may be well correlated with the XRD conclusions regarding the nano-assembly of very small CeO_2 nanoparticles on the LDH matrix. Accordingly, these CeO_2 nanoparticles cannot be observed with SEM technique indicating their small nanoparticle size. Further, we used the TEM technique to evidence the formation of very small CeO_2 nanoparticles and to investigate their dispersions on the LDH layers. The TEM image with the corresponding EDX chemical analysis of the assembled CeO_2/ZnTi-LDH sample (Fig. 3C and D) indicates the formation of highly dispersed CeO_2 nanoparticles, with regular shape and an average size of 5 nm.

Thermal stability and phase transformation in temperature was studied using TG/DTG method. Fig. 4 displays the DTG profiles of the ZnTi-LDH and CeO_2/ZnTi-LDH samples.

For the as-synthesized ZnTi-LDH sample, the first endothermic transition observed up to 100 °C corresponds to the water loss from the external surface and interlayer gallery. As reported before for the tetravalent-containing LDH structures, the lamellar structure has a decreased thermal stability and starts to dehydroxylate and decarbonatate in the range 200–300 °C. Another weight loss is observed between 400 °C and 500 °C which may be assigned to the conversion into a ZnO lattice, above this temperature the solid state diffusion of the cations with the formation of the spinel-type structure occurs. After the CeO_2 deposition on ZnTi-LDH, the structure of the obtained mixed oxide solution shows a weight loss at lower temperature, two small weight losses up to 600 °C and one major endothermic transition in the range 700–800 °C. The first weight loss may be assigned to the surface adsorbed water molecules. Two small transitions are observed between 300 and 600 °C which may be correlated with the conversion into an oxidic lattice. The weight loss observed at higher temperatures is most probably assigned to the removal of sulphate anions and full crystallization of the spinel-type structure. These observations were also confirmed using the XRD, Raman and UV–vis with Diffuse Reflectance Spectroscopy

Table 1
The influence of the synthesis and heat-treatment conditions on the phase composition and crystallite size.

Sample	ZnTi-LDH	ZnTi-600 °C	ZnTi-750 °C	CeO_2/ZnTi-LDH	CeO_2/ZnTi-600 °C	CeO_2/ZnTi-750 °C
[a]Phase/[b]crystallite size (nm)	LDH/5.3	ZnO/34.3 Zn_2TiO_4/9.06	ZnO/40.84 Zn_2TiO_4/36.3	CeO_2/nd LDH/nd	CeO_2/19.46 Zn_2TiO_4/17.36	CeO_2/40.54 Zn_2TiO_4/17.05

[a] Based on the XRD and Raman observations.
[b] Calculated using the Scherrer equation [20] and selecting the (0 0 3) plane for the LDH phase; (1 0 0) plane for the ZnO phase; (1 1 1) plane for the CeO_2 phase; (3 1 1) plane for the Zn_2TiO_4 phase. *nd* – not determined.
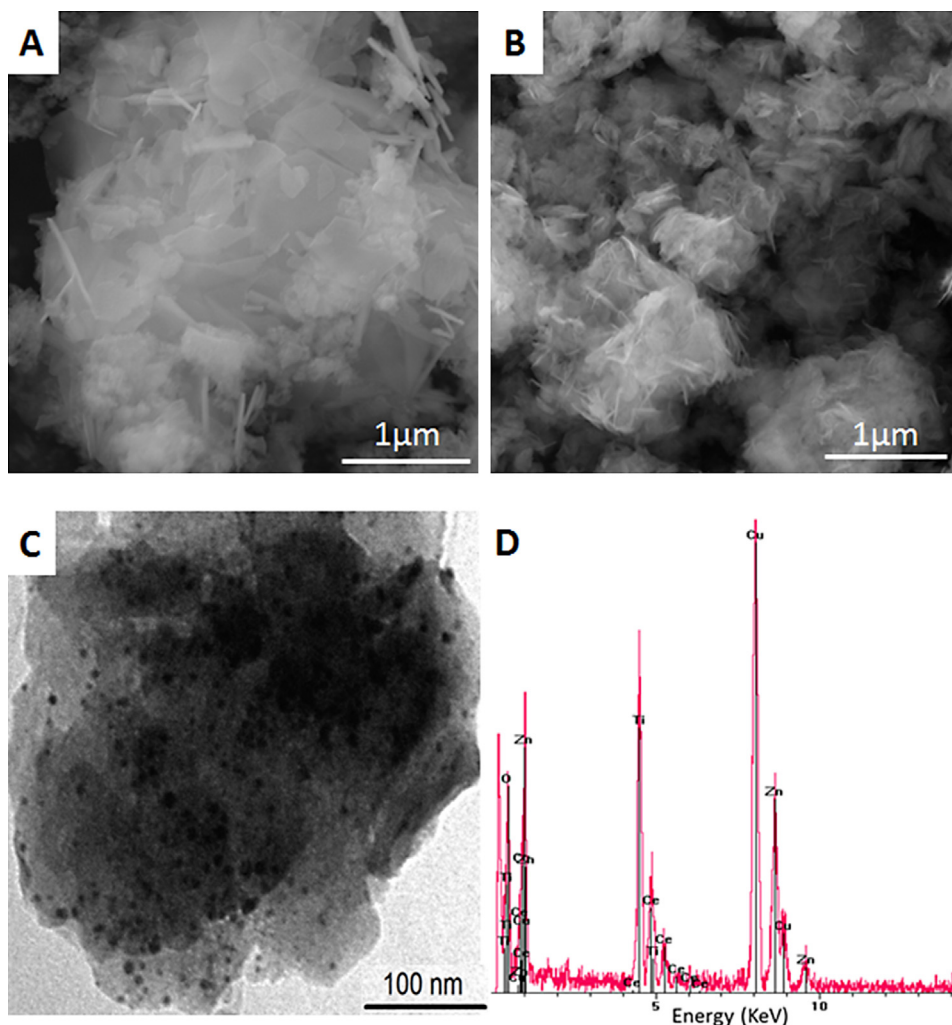
Fig. 3. Microscopic images of the most representative samples: SEM images of (A) ZnTi-LDH and (B) CeO$_2$/ZnTi-LDH samples; (C) TEM image and (D) EDX measurement of the CeO$_2$/ZnTi-LDH sample.

measurements on derived mixed oxides obtained by calcination at 600 °C and 750 °C.

The XRD data reveal that after the heat treatment at 600 °C (Fig. 1b), the ZnTi-LDH sample undergoes transformation mainly into a ZnO wurtzite-type lattice together with very small Zn$_2$TiO$_4$ (cubic) with inverse spinel crystal structure [22]. In the inverse spinel structure, half of Zn are at tetrahedral interstices and the remainder sharing octahedral interstices with Ti ions. Zn$_2$TiO$_4$ has been widely used as a regenerable catalyst as well as an important pigment in industry [23,24]. The Zn$_2$TiO$_4$ form is usually synthesized via solid-state reaction at high temperatures (typically above 1000 °C). Therefore, this may be regarded as an additional advantage of the synthesis method and the materials involved in this study, namely the possibility to obtain a well crystallized Zn$_2$TiO$_4$ inverse spinel structure under milder heating conditions. It was reported that ZnO/Zn$_2$TiO$_4$ coupled nanocomposite may provide better photo-oxidative effect than commercial Degussa P25 toward removal of dyes [25] or acetone [26]. Further calcination up to 750 °C leads to the complete crystallization with a concomitant growth of the coupled ZnO/Zn$_2$TiO$_4$ system (Table 1).

When the CeO$_2$ nanoparticles are supported on the ZnTi-LDH material, its structural characteristics together with the nature of the derived mixed oxides obtained under heat treatment are different. It is important to note that for the reconstruction step, the Cerium(IV) sulfate tetrahydrate, had a double role: to provide the

Ce^{4+} cations for the formation of the CeO$_2$ nanoparticles on the surface of the brucite-like layers by a self-assembly mechanism realized in a single and fast synthetic step, and secondly as anionic source in the reconstruction of the interlayer. This mechanism was thoroughly explored previously in our research group for the formation of highly dispersed metal and/or metal oxide nanoparticles on LDHs-type structures [4,15,16,27,28]. The choice of the sulfate salt of Ce^{4+} ions was based on the hypothesis that in temperature, the sulfate anions are lost at very high temperature [29] compared to other anions, e.g. nitrates, carbonates or acetylacetonates, and the layered structure if formed may have higher thermal stability.

In an initial stage of synthesis, when the synthesis strategy involving the *memory effect* property of these materials is involved, the XRD pattern (Fig. 2b) indicates that almost completely amorphous phases were obtained. Although not observed with the XRD technique, we assume that the layered structure is partly regenerated after this reconstruction step. In general, to observe a compound by X-ray diffraction it has to be present in more than 3%, the crystallite size has to be larger than ca. 2.5 nm and on the surface [18,30]. In our case, the very small crystallites with LDH structure are probably sheltered by amorphous phase or very small CeO$_2$ nanoparticles and could not be detected with X-ray diffraction [18]. In Raman spectroscopy, a band appears below these constrains, therefore Raman technique was used to demonstrate these assumptions and further explore the phase composition of
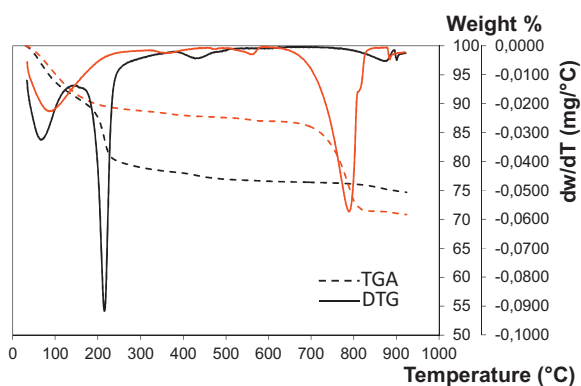
Fig. 4. The TGA/DTG profiles of ZnTi-LDH (black curves) and CeO$_2$/ZnTi-LDH (red curves) samples.

the obtained materials as well as the phase transformations in temperature. Fig. 5 displays the Raman spectra of some representative samples.

The Raman spectra of the reconstructed CeO$_2$/ZnTi-LDH sample (Fig. 5a) show seven main bands, with maxima at 399 cm^{-1}, 453 cm^{-1}, 565 cm^{-1}, 611 cm^{-1}, 715 cm^{-1}, 1008 cm^{-1} and 1062 cm^{-1}. The first two bands may be assigned to the vibration of the cation-oxygen bonds of the M(OH)$_x$ units (M = Zn or Ti) [31–33]. The next Raman bands may be regarded as a clear fingerprint of the presence of sulphate anions in the interlayer gallery of LDH regions [33]. The vibration modes centered at 1008 cm^{-1}, 1062 cm^{-1}, 715 cm^{-1} and 611 cm^{-1} may be assigned to the presence of the sulphate anions with a lowered symmetry. Bish et al. observed for honessite the sulphate υ_1, υ_2, υ_3 and υ_4 modes at 980 cm^{-1}, 500 cm^{-1}, 1140 cm^{-1} and 650 cm^{-1}, respectively [34]. The υ_3 mode is clearly split but no separate band positions were given. This is a clear evidence of the presence of the sulphate anions with lowered symmetry from T_d for the free anion to C_3 or C_{3v} in a restricted environment in the interlayer gallery, which generates the splitting of the υ_3 mode. A shoulder is observed at 464 cm^{-1} corresponding to the F$_{2g}$ vibration for the cubic fluorite structure indicating the presence of very fine CeO$_2$ nanoparticles on the surface of the reconstructed sample [35]. When the sample is calcined at 600 °C, the Raman spectra profile shows the presence of a very intense vibration band at 464 cm^{-1} indicating the complete crystallization and growth of the CeO$_2$ nanoparticles. The vibrations characteristic for the Zn–OH units and the Ti–OH units are now observed like low intensity shoulders indicating that the LDH structure is changing into a solid solution with a good ordering of the cations. It is interesting to note that the characteristic fingerprint vibrations of the sulphate anions are decreased in
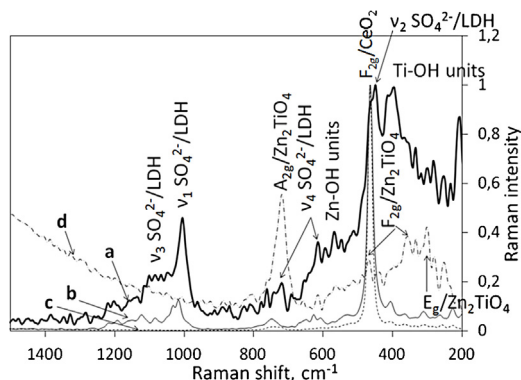
intensity but did not disappear supporting our hypothesis of higher thermal stability of the obtained LDH-type material. Small vibrations at 721 cm^{-1} associated with the A$_g$ vibration of the Zn$_2$TiO$_4$ inverse spinel structure starts to appear at this moment. These findings may be well correlated with the XRD and DTG observations showing that at 600 °C the solid state reaction starts with the concomitant formation of the spinel type structure. The υ_1 and υ_3 vibrations of the sulphate anions completely disappear after the heat treatment at 750 °C (Fig. 5c) which may be well correlated with the DTG observations suggesting that at this temperature the sulphate anions are eliminated, the layered structure collapses and the spinel type lattice completely crystallizes. The characteristic vibrations A$_g$, F$_{2g}$ and E$_g$ associated with the Zn$_2$TiO$_2$ inverse spinel structure are clearly observed in the Raman spectra of the ZnTi-750 °C sample [23]. It is important to note that in the case of the ZnTi-750 °C sample, the intense Raman A$_g$ vibration (with very low intensity in the CeO$_2$/ZnTi-calcined samples) suggests different geometry/configuration as indicated by the Raman selection rules. The Zn$_2$TiO$_2$ nanoparticles geometry is changing from VV in the ZnTi-750 °C sample, characterized by very strong 721 cm^{-1} phonon mode, to VH configuration for the CeO$_2$/ZnTi-calcined samples [23]. Therefore, this is an indication of the presence of indirect transitions of the Zn$_2$TiO$_4$ mainly due to the contribution of the 721 cm^{-1} phonon [23].

The UV–vis Diffuse Reflectance Spectroscopy was used to investigate the environment, phase composition and evaluation of the band gap energies of the obtained coupled nano-sized photocatalytic systems. The UV–vis DR spectra of the representative samples are shown in Fig. 6. The parent ZnTi-LDH sample (Fig. 6A, (a)) exhibits an absorption band at lower wavelengths up to 350 nm which can be assigned to the ligand-to-metal charge transfer involving Zn and Ti atoms in octahedral coordination within the layered network [4,36]. As observed also with XRD technique, the heat treatment of this sample at 600 °C starts to produce changes in the phase composition forming ZnO nanoparticles in combination with small Zn$_2$TiO$_4$ inverse spinel-type structure. These transformations are also producing changes into the absorption spectra, with concomitant change in the energy band levels. Further heat treatment up to 750 °C leads to a complete modification in the energy band levels. The band gap energies were calculated using the wavelength of the absorption edges. These were determined by extrapolating the sharply rising and horizontal portions of the UV–vis curves and defining the edges as the wavelengths of the intersection [18].

The UV–vis DR profiles (Fig. 6A) confirm the formation of the ZnO nanoparticles and the band gap energy value of 3.16 eV is not influenced by the calcination temperature, which is in agreement with the literature reports for the ZnO nanoparticles [18,37]. It also indicates the formation of the inverse spinel-type Zn$_2$TiO$_4$ and the formation of an additional band energy level characterized by an absorption at lower wavelengths and an indirect band gap energy of 3.52 eV [38]. The formation of the indirect band gap material was also demonstrated with Raman spectroscopy. The 721 cm^{-1} phonon (A$_g$) participates in the electron transitions from the top of the O^{2-} 2p valence band to the bottom of the Ti^{4+} t$_{2g}$ or Zn^{2+} 4s conduction band [23]. The UV–vis DR spectra of the CeO$_2$ supported ZnTi-LDH samples show different profile indicating changes in the structural characteristics as well as on the energy band levels.

A first observation is that the UV–vis DR spectra of both CeO$_2$/ZnTi-LDH and CeO$_2$/ZnTi-600 °C samples confirm the conclusions withdrawn from the Raman analysis, showing the combination of the layered structure, with an absorption band at lower wavelength (Zn^{2+} and Ti^{4+} in octahedral environment in the LDH phase), together with the cerium oxide nanoparticles causing the shift of the absorption profile toward higher wavelengths, e.g. about 80 nm as compared to ZnO (Fig. 6B with the corresponding band component analysis in Fig. 6C and D).
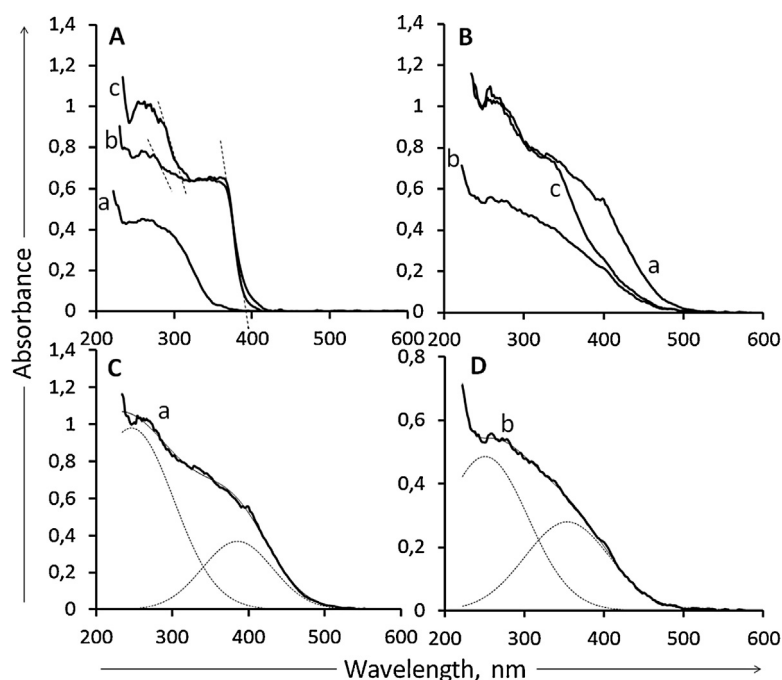

Fig. 5. Raman spectra of (a) CeO$_2$/ZnTi-LDH, (b) CeO$_2$/ZnTi-600 °C, (c) CeO$_2$/ZnTi-750 °C and (d) ZnTi-750 °C samples.

Fig. 6. The UV–vis diffuse reflectance spectra of (A) (a) ZnTi-LDH, (b) ZnTi-600 °C and (c) ZnTi-750 °C and (B) (a) CeO$_2$/ZnTi-LDH, (b) CeO$_2$/ZnTi-600 °C and (c) CeO$_2$/ZnTi-750 °C samples; (C) and (D) band component analysis of the (a) spectra of the CeO$_2$/ZnTi-LDH and (b) spectra of the CeO$_2$/ZnTi-600 °C in figure (B), respectively.
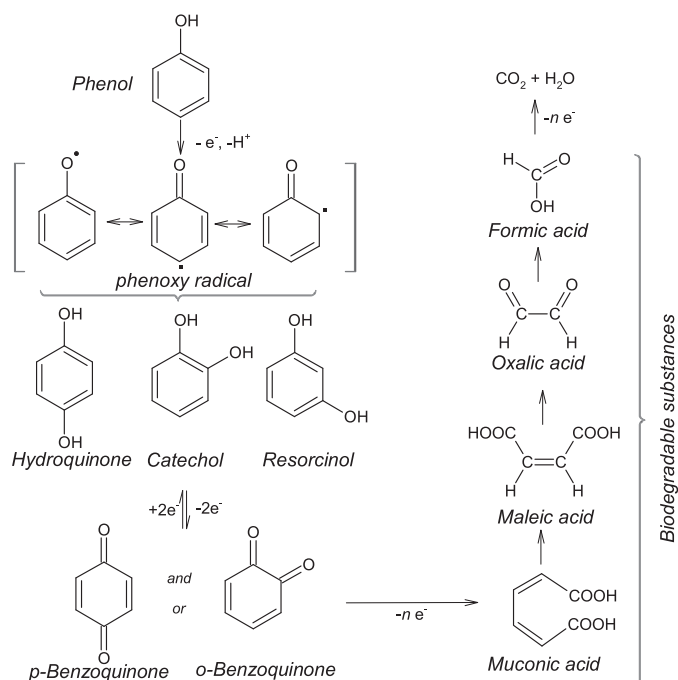
Another observation is that the absorption profile corresponding to the cerium species is blue shifted to lower wavelength after the calcination at 600 °C comparing to the uncalcined sample (see Fig. 6B spectra a and b). As stated before, due to its low redox potential a Ce easily passes from Ce^{4+} to Ce^{3+} ionic state, and this probably occurred in a higher ratio immediately after the reconstruction step. Thus, this absorption behavior may be interpreted by taking into account the possibility that before calcination a higher fraction of Ce^{3+} cations exist in this sample [39], which further oxidizes upon calcination and changes into Ce^{4+} cations, respectively. Moreover, the spectra manifest a lower intensity in the low wavelength region which may be associated to the decrease of the changing of the layered structure into the solid solution with well-ordered cations, and may be well correlated with the Raman observations. These findings may be very important when the obtained photocatalysts will be tested for their efficiency for the phenol removal, and can be correlated with the different photodegradation pathways as it will be discussed in detail in a later section.

Further heat treatment up to 750 °C leads to the formation of the coupled CeO$_2$/Zn$_2$TiO$_4$ system showing two edge absorption profile of the UV–vis DR spectra (Fig. 6B (c)) [8,23]. The calculated value of 3.0 eV for band gap energy of the CeO$_2$ nanoparticles is consistent with the values reported in the literature [8]. It indicates the presence of Ce atoms (in either the 3+ or 4+ state) on the external surface leading to oxygen vacancies and defects whose influence on the band gap overcomes the expected influence of the regular quantum size effect [8]. Another aspect of particular importance is the significant change in the band gap energy associated with the formation of an direct band gap Zn$_2$TiO$_4$ nanoparticles [23]. When the sample is calcined at 750 °C, the calculated value for the band gap energy is 3.11 eV and may be interpreted by taking into account the quantum size effect and also correlated with the smaller crystallite size observed also with XRD (Table 1). This effect was previously reported by Suwanboon et al. [40] when the band gap energy of Zn$_2$TiO$_4$ decreased when exposing at lower temperatures with concomitant decrease of the crystallite sizes. It is also indicating the presence of some defects in the electronic band of the Zn$_2$TiO$_4$ nanoparticles. These defects affect the optical properties of

the obtained photocatalytic system, their concentration increasing with the decrease of the band gap energy [40], and this may also have an effect on the photodegradation efficiency of the obtained coupled semiconductor oxides.

3.2. Photocatalytic evaluation of the obtained catalysts

As illustrated in Scheme 1, the mechanism of oxidative mineralization of phenol involves first the formation of highly toxic quinones and then the subsequent opening of the aromatic ring

Scheme 1. The schematic representation of the degradation process of phenol.
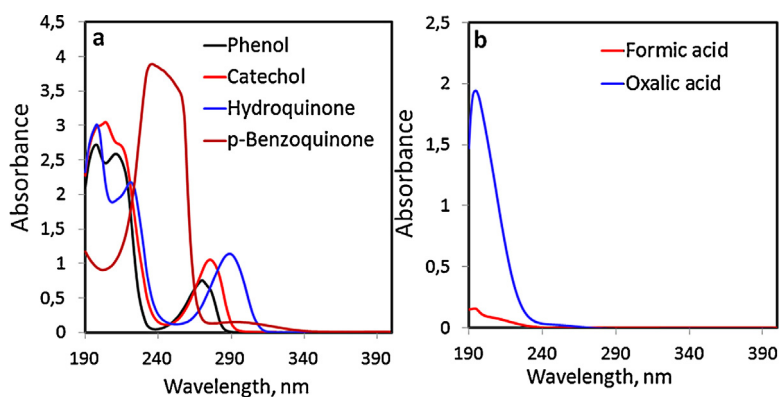
Fig. 7. UV–vis spectra of the pure reagents (50 mg/L): (a) aromatic and (b) aliphatic compounds mainly observed during the photo-oxidation process of phenol under UV light.

leading to the formation of biodegradable aliphatic acids, and finally mineralization to carbon dioxide and water [41]. It is very important to establish the relative proportions between the aliphatic acids and the aromatic compounds since through this factor it would be possible to determine when a given sample becomes harmless from the toxicological point of view [42].

The main compounds observed in our photocatalytic tests were the aromatic compounds: Catechol, Hydroquinone, p-Benzoquinone and the aliphatic products: oxalic and formic acids, respectively. In order to judge the composition of the mixtures resulted from the photocatalytic reactions, standard solutions of the above specified pure reagents (50 mg/L) were analyzed using the UV–vis spectrophotometry and the results are presented in Fig. 7. It is easy to observe from this figure that, even in the absence of phenol, the absorbance signal will be different from zero in the presence of any intermediary of the photochemical degradation process.

Therefore, UV–vis spectrophotometry was used to explain the evolution of the phenol photodegradation process. The catalytic tests were realized at a catalyst dose of 1 g/L using both series of samples, e.g. ZnTi-LDH and CeO$_2$/ZnTi-LDH and the derived mixed oxides obtained after the controlled thermal treatment. The following results will show that the obtained photocatalysts degrade phenol, but the efficiency and the mixture of intermediates are different for the unsupported and supported CeO$_2$ on ZnTi-LDH material. The different behavior may be attributed to the formation of different coupled photocatalytic systems as it was described in detail in the characterization section.

3.2.1. Photocatalytic evaluation of the ZnTi-LDHs systems

The photocatalytic process can be visualized in Fig. 8. Initially, the phenol solution (50 mg/L) was stirred without UV light for 30 min in order to establish the adsorption–desorption equilibrium between the phenol and the catalyst surface. During this time, no modification in the absorption profile of phenol solution was observed. After the UV radiation was turned on, the absorption profile becomes broader in the case of the ZnTi-LDH sample (Fig. 8a), and even more intense for the derived mixed oxides obtained after calcination at 600 °C and 750 °C, respectively. This can be interpreted as the beginning of the photodegradation process and the formation of the free radicals. The main intermediary aromatic product formed is catechol as it absorbs in the same region broadening the absorption profile.

The difference in the intensity of the broad absorption profile observed for the calcined samples compared with the initial ZnTi-LDH sample may be attributed to the difference in structure and phase composition of the obtained materials. Initially, the ZnTi-LDH sample contains the ZnO$_6$ and TiO$_6$ octahedra sharing edges

forming the characteristic brucite-like sheets in a layered double hydroxide. For this sample, a mixture of phenol and catechol is obtained in the first minutes of reaction, after this moment the complete transformation of phenol in catechol and the subsequent aliphatic products being observed. The changes in the phenolic solution composition were highlighted by colors in the figures illustrating the photocatalytic tests. The derived calcined products are a combination of ZnO/Zn$_2$TiO$_4$ having a semiconductor type behavior producing a hyperchromic shift in the UV spectrum with concomitant electronic modifications on the phenol molecule indicating the formation of intermediary species with a different chromophore group. Therefore, in the first minutes of reaction, all the phenol molecules are immediately transformed in catechol which can be degraded to biodegradable aliphatic acids. Consequently, the apparent concentration increases (Fig. 8b and c), but this can be interpreted as a complete transformation in catechol.

The degradation process continues by the opening of the catechol ring and forming the corresponding aliphatic acids as described in Scheme 1. The main aliphatic acids observed in the absorption profile are oxalic and formic acids showing an absorption maximum at 198 nm and 195 nm, respectively. The ZnTi-LDH sample seems to be the most effective catalyst. Nevertheless, in this case the difference between these catalysts is not as significant, the photodegradation process following the same pathway toward phenol removal from aqueous solutions.

3.2.2. Photocatalytic evaluation of the CeO$_2$/ZnTi-LDHs systems

The photocatalytic degradation of phenol by the CeO$_2$/ZnTi-LDHs nanocomposite systems may be visualized in Fig. 9.

For these series of samples, the phenol photodegradation occurs differently and this can be associated with the presence of the CeO$_2$ nanoparticles on the obtained photocatalysts. These differences also appear from the first step in the photodegradation tests, when the absorption in dark produces some changes in the phenolic solution. For the uncalcined CeO$_2$/ZnTi-LDH sample, the adsorption step occurs normally, without significant modification in the absorption profile (Fig. 9a). When the UV radiation is turned on, the formation of a mixture of aromatic and aliphatic fractions, e.g. hydroquinone, catechol, muconic and oxalic acids, respectively. Thus, accordingly to the proposed mechanism presented in Scheme 1, a part of the initial phenol molecules opens the aromatic ring and degrades to aliphatic muconic, oxalic and formic acids and finally CO$_2$ and H$_2$O as final mineralization products. The hydroquinone fraction undergoes fast transformation into p-benzoquinone, a very stable molecule. Only small part of this molecule is degraded until the end of the photocatalytic test.

Differences are observed when the samples are calcined at different temperature. As observed with TG/DTG technique, this
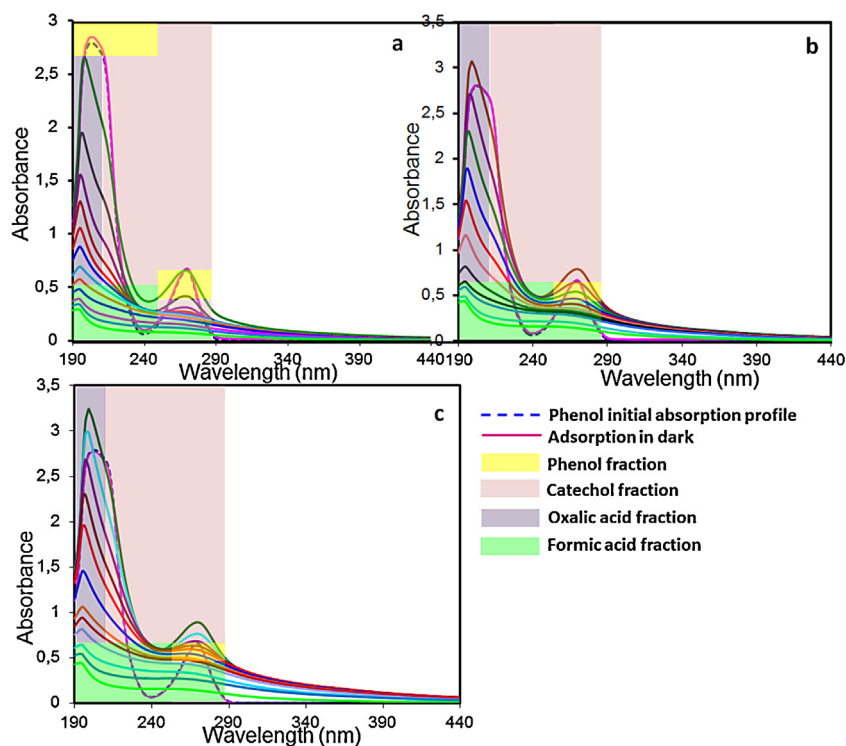
Fig. 8. UV–vis spectra of phenol photo-oxidation process in the presence of (a) ZnTi-LDH, (b) ZnTi-600 °C and (c) ZnTi-750 °C samples.

sample undergoes different phase transformation in temperature as compared with the parent ZnTi-LDH sample. An additional small weight loss was observed up to 400 °C, which probably did not cause any structural changes in the obtained photocatalytic system. To prove this assumption, an additional photocatalytic test was realized on a sample calcined at 400 °C (Fig. 9b). For the CeO₂/ZnTi-600 °C sample, after the absorption step in dark, an combined hypsochromic and hyperchromic effect is observed indicating that

the electronic modifications are starting to occur even before UV irradiation. The apparent concentration increases, but this can be interpreted by the formation of different chromophore groups with the formation of a mixture of catechol, hydroquinone with subsequent transformation in muconic, oxalic and formic acids and p-benzoquinone, respectively. The results obtained testing the CeO₂/ZnTi-400 °C sample suggest the same behavior suggesting no structural transformations from 400 °C up to 600 °C.
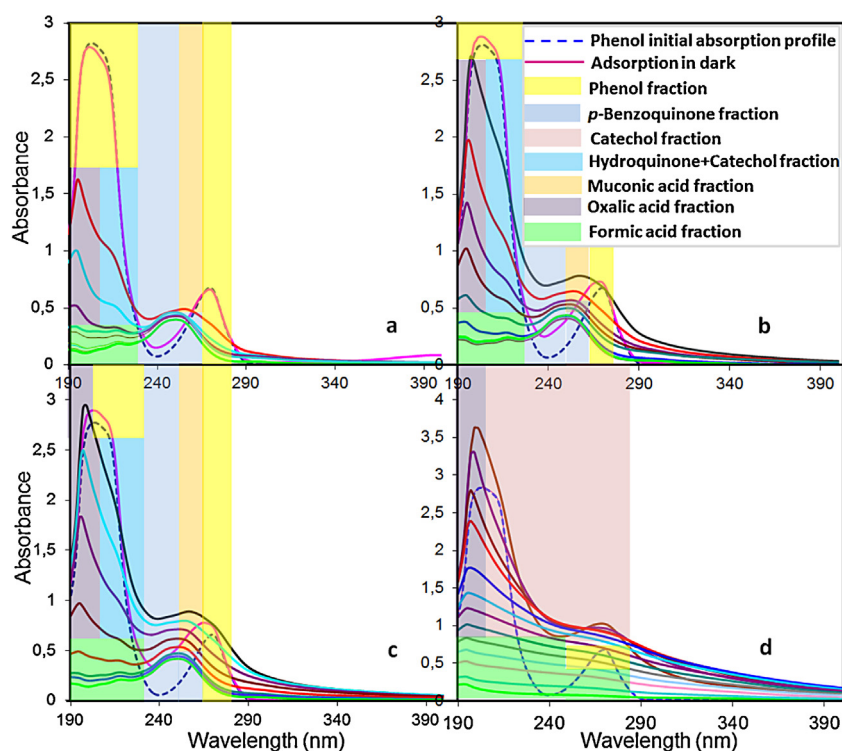

Fig. 9. UV–vis spectra of phenol photo-oxidation process in the presence of (a) CeO₂/ZnTi-LDH, (b) CeO₂/ZnTi-400 °C, (c) CeO₂/ZnTi-600 °C and (d) CeO₂/ZnTi-750 °C samples.
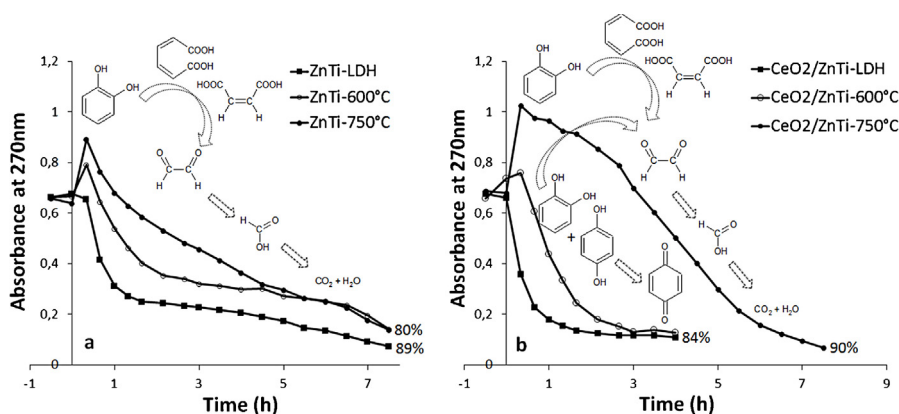
Fig. 10. Degradation of phenol under UV light using (a) ZnTi-LDH and (b) CeO$_2$/ZnTi-LDH samples.

On the contrary, when the sample is calcined at 750 °C, the photocatalytic test shows different pathway of the mineralization process. This may be strongly related with the formation of the CeO$_2$/Zn$_2$TiO$_4$ nanocomposite system which manifests different semiconductor behavior. These changes may be well correlated with the observations withdrawn from the Raman and UV–vis DR data indicating differences in the band gap energy of the generated combined nanostructures. It can be observed in Fig. 9d that after the adsorption step in dark, no modification in the electronic structure of phenol molecule occurs, the UV–vis absorption profile overlapping with the one measured for the initial phenol solution. After the UV radiation is turned on, the electronic structure immediately changes due to the hyperchromic effect with the concomitant apparent increase in the concentration. This can be interpreted by the complete transformation in catechol which allows the opening of the aromatic ring and the complete mineralization of phenol.

An overview of the phenol photodegradation process can be observed in Fig. 10, where the decrease of the absorbance at 270 nm (maximum absorption wavelength characteristic for phenol) is plotted against time. The proposed pathways are also schematically illustrated. Comparing the two photocatalytic systems described in this study, the best efficiency of phenol removal was observed for the CeO$_2$/ZnTi-LDH and calcined samples. In can be observed that 90% of phenol is completely removed by the CeO$_2$/ZnTi-750 °C. Although the process takes longer than for the uncalcined CeO$_2$/ZnTi-LDH and CeO$_2$/ZnTi-600 °C samples, the resulting degradation slurry contains no traces of p-benzoquinone, the mineralization products being CO$_2$ and water.

Valente et al. previously reported the deposition of CeO$_2$ nanoparticles on a MgAl-layered double hydroxide with application in the photocatalytic elimination of phenol in aqueous solution and the maximum efficiency of phenol removal was found to be ∼50% [19].

Therefore, it may be concluded that the brucite-type layer composition has a major effect on the obtained coupled systems. Moreover, the advantage of using a LDH type support for the deposition of metal and/or metal oxide nanoparticles stands in the versatility of the brucite-like sheets composition which may allow the insertion of key cations, like Zn^{2+} and Ti^{4+}, within the LDH network, supply a good dispersion of the metal cations within the layers and act as charge separation centers enhancing the efficiency in subsequent applications.

4. Conclusions

Layered double hydroxide containing zinc and titanium was prepared using coprecipitation method at constant pH. Furthermore, the self-assembly of CeO$_2$ nanoparticles and ZnTi-LDH were

obtained by taking advantage of the remarkable *memory effect* property of this type of material. It was demonstrated that the layered structure could be regenerated and the obtained nanosized CeO$_2$ – ZnTi-LDH self-assembly can form under mild temperature conditions combined nanosized CeO$_2$/Zn$_2$TiO$_4$ photocatalytic system with specific properties. The photocatalytic efficiency of the obtained products was evaluated for the degradation of phenol under UV irradiation. The phenol degradation pathway was rationalized using UV–vis spectroscopy. This technique proved to be very useful to identify the intermediates formed during the reaction. It was found that the brucite-type layer composition has a major effect on the obtained coupled systems. The advantage of using a LDH type matrix assembled to metal oxide nanoparticles stands in the versatility of the brucite-like sheets composition which may allow the insertion of key cations, like Zn^{2+} and Ti^{4+}, within the LDH network. The LDH materials can supply a good dispersion of the metal cations within the layers which may act as charge separation centers enhancing the efficiency in subsequent applications.

References

[1] M. Qamar, M. Muneer, D. Bahnemann, Journal of Environmental Management 80 (2006) 99–106.
[2] D.D. Dionysiou, A.P. Khodadoust, A.M. Kern, M.T. Suidan, I. Baudin, J.-M. Laîné, Applied Catalysis B: Environmental 24 (2000) 139–155.
[3] V.M. Brown, D.H.M. Jordan, B.A. Tiller, Water Research 1 (1967) 587–594.
[4] E.M. Seftel, M. Mertens, P. Cool, Applied Catalysis B: Environmental 134–135 (2013) 274–285.
[5] E.M. Seftel, E. Popovici, M. Mertens, E.A. Stefaniak, R. Van Grieken, P. Cool, E.F. Vansant, Applied Catalysis B: Environmental 84 (2008) 699–705.
[6] J. Reddy, V. Durga Kumari, M. Subrahmanyam, Catalysis Letters 123 (2008) 301–306.
[7] T. López, F. Rojas, R. Alexander-Katz, F. Galindo, A. Balankin, A. Buljan, Journal of Solid State Chemistry 177 (2004) 1873–1885.
[8] A. Corma, P. Atienzar, H. Garcia, J.-Y. Chane-Ching, Nature Materials 3 (2004) 394–397.
[9] J. Fang, X. Bi, D. Si, Z. Jiang, W. Huang, Applied Surface Science 253 (2007) 8952–8961.
[10] A. Urdă, I. Popescu, T. Cacciaguerra, N. Tanchoux, D. Tichit, I.-C. Marcu, Applied Catalysis A: General 464–465 (2013) 20–27.
[11] B. Jiang, S. Zhang, X. Guo, B. Jin, Y. Tian, Applied Surface Science 255 (2009) 5975–5978.
[12] S. Song, L. Xu, Z. He, H. Ying, J. Chen, X. Xiao, B. Yan, Journal of Hazardous Materials 152 (2008) 1301–1308.
[13] G. Águila, F. Gracia, P. Araya, Applied Catalysis A: General 343 (2008) 16–24.

[14] H. Tong, S. Ouyang, Y. Bi, N. Umezawa, M. Oshikiri, J. Ye, Advanced Materials 24 (2012) 229–251.
[15] G. Carja, L. Dartu, K. Okada, E. Fortunato, Chemical Engineering Journal 222 (2013) 60–66.
[16] G. Carja, E. Husanu, C. Gherasim, H. Iovu, Applied Catalysis B: Environmental 107 (2011) 253–259.
[17] F. Cavani, F. Trifirò, A. Vaccari, Catalysis Today 11 (1991) 173–301.
[18] E.M. Seftel, E. Popovici, M. Mertens, K.D. Witte, G.V. Tendeloo, P. Cool, E.F. Vansant, Microporous and Mesoporous Materials 113 (2008) 296–304.
[19] J.S. Valente, F. Tzompantzi, J. Prince, Applied Catalysis B: Environmental 102 (2011) 276–285.
[20] E.M. Seftel, E. Popovici, M. Mertens, G. Van Tendeloo, P. Cool, E.F. Vansant, Microporous and Mesoporous Materials 111 (2008) 12–17.
[21] L. Teruel, Y. Bouizi, P. Atienzar, V. Fornes, H. Garcia, Energy & Environmental Science 3 (2010) 154–159.
[22] H.J. Fan, Y. Yang, M. Zacharias, Journal of Materials Chemistry 19 (2009) 885–900.
[23] L. Li, F. Li, T. Cui, Q. Zhou, D. Xu, Physica Status Solidi A 209 (2012) 2596–2599.
[24] Y. Yang, R. Scholz, H.J. Fan, D. Hesse, U. Gösele, M. Zacharias, ACS Nano 3 (2009) 555–562.
[25] A.R.M.S. Janitabar-Darzi, A. Ghaemi, World Academy of Science, Engineering and Technology 52 (2011) 524–525.
[26] L. Wan, X. Li, Z. Qu, Y. Shi, H. Li, Q. Zhao, G. Chen, Journal of Hazardous Materials 184 (2010) 864–868.
[27] G. Carja, G. Lehutu, L. Dartu, M. Mertens, P. Cool, Applied Clay Science 65–66 (2012) 37–42.
[28] G. Carja, H. Chiriac, N. Lupu, Journal of Magnetism and Magnetic Materials 311 (2007) 26–30.
[29] R.L. Frost, M.L. Weier, M.E. Clissold, P.A. Williams, J.T. Kloprogge, Thermochimica Acta 407 (2003) 1–9.
[30] J.A. Rivera, G. Fetter, Y. Jiménez, M.M. Xochipa, P. Bosch, Applied Catalysis A: General 316 (2007) 207–211.
[31] J.C. Villegas, O.H. Giraldo, K. Laubernds, S.L. Suib, Inorganic Chemistry 42 (2003) 5621–5631.
[32] R.L. Frost, C. Pinto, Journal of Raman Spectroscopy 38 (2007) 841–845.
[33] F.F.C. Ardau, P.C. Ricci, C. Cannas, E. Dore, P. Lattanzi, Mine Water – Managing the Challenges, Aachen, Germany, 2011, pp. 559–562.
[34] D.L.B.A.A. Livingstone, Mineralogical Magazine 44 (1981) 339–343.
[35] Q.-H. Xu, D.-M. Xu, M.-Y. Guan, Y. Guo, Q. Qi, G.-D. Li, Sensors and Actuators B: Chemical 177 (2013) 1134–1141.
[36] N. Das, A. Samal, Microporous and Mesoporous Materials 72 (2004) 219–225.
[37] C. Wang, X. Wang, B.-Q. Xu, J. Zhao, B. Mai, P.A. Peng, G. Sheng, J. Fu, Journal of Photochemistry and Photobiology A: Chemistry 168 (2004) 47–52.
[38] C. Wang, B.-Q. Xu, X. Wang, J. Zhao, Journal of Solid State Chemistry 178 (2005) 3500–3506.
[39] F.B. Li, X.Z. Li, M.F. Hou, K.W. Cheah, W.C.H. Choy, Applied Catalysis A: General 285 (2005) 181–189.
[40] S. Suwanboon, P. Amornpitoksuk, P. Bangrak, Ceramics International 37 (2011) 333–340.
[41] C. Borras, C. Berzoy, J. Mostany, J.C. Herrera, B.R. Scharifker, Applied Catalysis B: Environmental 72 (2007) 98–104.
[42] R. Vargas, C. Borrás, J. Mostany, B.R. Scharifker, Water Research 44 (2010) 911–917.